Three-Dimensional Navier-Stokes Simulations of Turbine Rotor-Stator Interaction; Part I – Methodology

Man Mohan Rai*
NASA Ames Research Center, Moffett Field, California

Fluid flows within turbomachinery tend to be extremely complex. Understanding such flows is crucial to efforts to improve current turbomachinery designs, and the computational approach can be used to great advantage in this regard. This study presents a finite-difference, unsteady, thin-layer Navier-Stokes approach to calculating the flow within an axial turbine stage. The relative motion between the stator and rotor airfoils is made possible with the use of patched grids that move relative to each other. The calculation includes end-wall and tip-leakage effects. The numerical methodology is presented in detail in the present paper (Part I). The computed results and comparisons of these results with experimental data are presented in a companion paper (Part II).

Nomenclature

$\tilde{A},\tilde{B},\tilde{C}$ = inviscid flux vector Jacobians
c = local speed of sound
E,F,G = inviscid flux vectors
$\tilde{E},\tilde{F},\tilde{G}$ = transformed inviscid flux vectors
e = total internal energy per unit volume
J = Jacobian of transformation
$\tilde{M},\tilde{N}$ = viscous flux vector Jacobians
Pr = Prandtl number
p = pressure
Q = vector of dependent variables
$\tilde{Q}$ = transformed dependent variable vector
q = magnitude of velocity
R,S,T = viscous flux vectors
$\tilde{R},\tilde{S},\tilde{T}$ = transformed viscous flux vectors
Re = Reynolds number
r = radial location from center of hub
s = entropy
t = time
u,v,we = Cartesian velocity components in the x,y,z directions, respectively
x,y,z = Cartesian physical coordinates
γ = ratio of specific heats
λ = coefficient of bulk viscosity
μ = dynamic viscosity
ξ,η,ζ = coordinates in computational space
ρ = density
τ = computational time
τ_{xx}, τ_{xy}, etc. = viscous stresses

Introduction

AN accurate numerical analysis of the flows associated with rotor-stator configurations can be very helpful in optimizing the performance of turbomachinery. However, such analyses tend to be computationally expensive and extremely complex because 1) the flow is inherently unsteady, 2) the geometries involved are complicated, 3) the flow periodically transitions between laminar and turbulent flow, and 4) there is relative motion between the stator and rotor rows. Nevertheless, a clear understanding of the aerodynamic processes associated with turbomachinery can aid the design process considerably; hence, the rather large computer costs of simulating the three-dimensional unsteady flows associated with turbomachinery are completely justified.

Several calculations of cascade flow have already been reported in the literature. These studies include two- and three-dimensional calculations using both the Euler and Navier-Stokes equations. References 1-5 constitute a typical cross section of the work done previously, but are by no means a complete review of earlier efforts. Although analyses of flows through isolated rows can be used to study many of the fluid mechanical phenomena in turbomachinery, such analyses yield no information regarding the unsteadiness arising out of the interaction of moving and stationary rows of airfoils. These interaction effects become increasingly important as the distance between successive rows is decreased. The experimental results of Ref. 6 show that the temporal pressure fluctuation near the leading edge of the rotor can be as much as 72% of the exit dynamic pressure when the axial gap is reduced to 15% of the chord length (for the operating conditions and geometry chosen). Thus, the need for treating the rotor and stator airfoils as a system when interaction effects are predominant is obvious.

From a computational point of view, one major difficulty in simulating rotor-stator flows arises because of the relative motion of the rotor and stator airfoils. A single grid that wraps around both the rotor and stator would have to distort considerably to accommodate the motion of the rotor and could result in inaccurate calculations. For small values of the axial gap between the rotor and stator airfoils, such an approach may even be altogether impractical. The obvious solution to this problem is to use several grids that move relative to each other. Typically, one would use a set of stationary grids to envelop the stator airfoils and a set of moving grids (stationary with respect to the rotor) to envelop the rotor airfoils. Information is then transferred between the several grids used, with the help of specialized boundary conditions.

Reference 7 presents rotor-stator-interaction results obtained using the Euler equations. The various natural boundary conditions such as inlet, discharge, blade surface, and periodicity boundary conditions that are required for rotor-stator calculations are presented, and the unsteady flow through a fan stage is calculated. However, there are several areas that have not been addressed in Ref. 7: 1) a general method of information transfer between the multiple grids employed, 2) viscous effects, and 3) the three-dimensionality of the flow. Viscous effects can contribute significantly toward the unsteady component of the flow because of the passage of

Presented as Paper 87-2058 at the AIAA/SAE/ASME/ASEE 23rd Joint Propulsion Conference, San Diego, CA, June 29-July 2, 1987; received Dec. 8, 1987; revision received June 20, 1988.

*Research Scientist. Associate Fellow AIAA.

the second set of airfoils through the wakes of the first set. End-wall and tip-leakage effects and the geometry of the airfoils may contribute significantly to the three-dimensionality of the flow. Hence, an accurate simulation of the flow within turbomachinery requires the time-accurate solution of the unsteady Navier-Stokes equations in three-dimensions.

In the multiple-grid approach, the calculation is performed on several grids that are either patched together (Fig. 1a) or overlaid (Fig. 1b). The boundary conditions used to transfer information from one grid to another must satisfy several requirements before they can be used effectively. The boundary conditions must, for example, be 1) numerically stable, 2) spatially and temporally accurate, 3) easily applicable in generalized coordinates, and 4) conservative so that flow discontinuities can move from one grid to another without any distortion. The conservative property although desirable is not required in the case of flows without discontinuities.

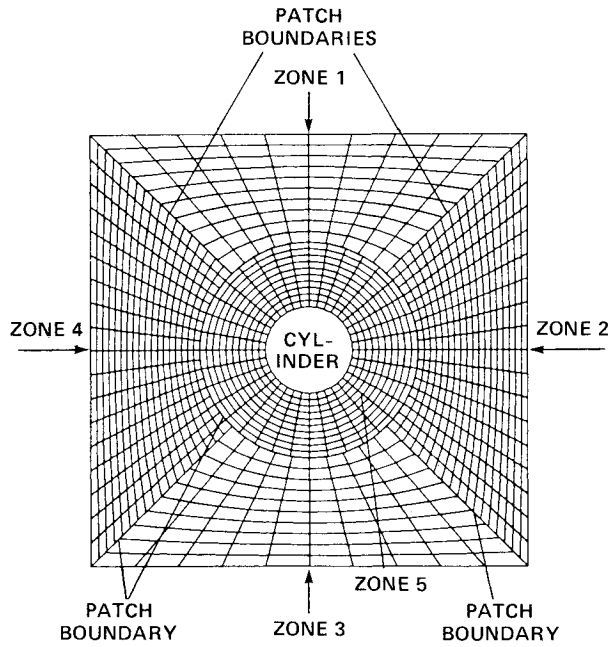

a) Example of patched grids

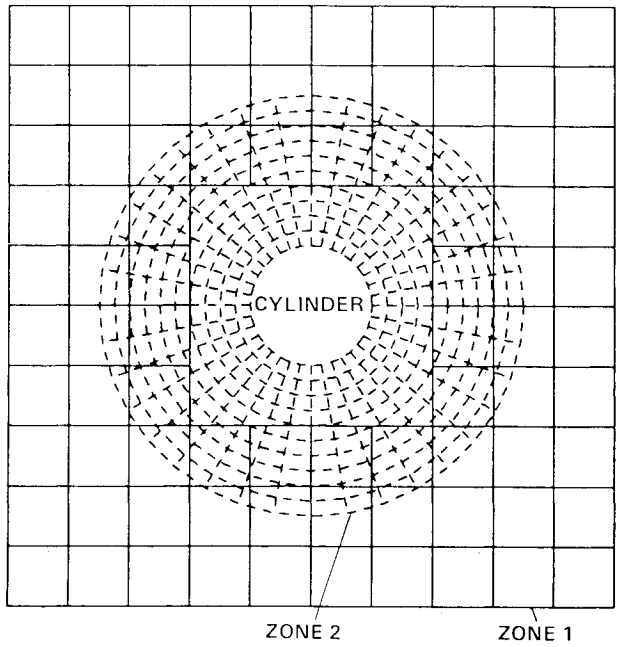

b) Example of overlaid grids

Fig. 1 Use of multiple grids in finite-difference calculations.

The boundary conditions required to transfer information from patch to patch in the patched-grid approach (Fig. 1a) are developed in detail in Refs. 8–10. In Ref. 8, a conservative patch boundary condition is developed for first-order-accurate explicit schemes. Results demonstrating the conservative property of the new boundary condition and the quality of solutions possible with patched grids are presented. In Refs. 9 and 10, this boundary condition is extended to work with implicit second-order-accurate schemes. The modifications to the boundary scheme that are required in order to transfer information between two patches that are moving relative to each other are also developed in Refs. 9 and 10. Preliminary results for a rotor-stator configuration are presented in Ref. 10.

The patched-grid technique as developed in Refs. 8–10 is used in Ref. 11 to simulate the flow past the rotor-stator configuration of an axial turbine. The airfoil geometry and flow conditions used are the same as those in Ref. 6. The unsteady, thin-layer Navier-Stokes equations are solved in a time-accurate manner to obtain the unsteady flowfield associated with this configuration. The numerically obtained results are compared with the experimental results of Ref. 6. A good comparison of theory and experiment is obtained in the case of time-averaged pressures on the rotor and stator. Pressure amplitudes (corresponding to the pressure variation in time) were also found to compare well with experiment, thus indicating the validity of the computed unsteady component of the flow.

More recently, a shearing-grid technique in which a single gird wraps itself around the rotor and stator and shears in order to effect the relative motion between stator and rotor airfoils has been used to solve the flow in a compressor stage.[12] The data from the sheared grid are interpolated onto an undistorted initial grid at points in time when the distortion exceeds a certain tolerance level. This approach seems to have the advantage of requiring less computing time per step (since zonal information transfer techniques are no longer required) but may be difficult to use when the axial gap between airfoils is small (less than 25% chord).

Two approximations were made in obtaining the results of Ref. 11. The first was a rescaling of the rotor geometry. The experimental turbine of Ref. 6 has 22 stator airfoils and 28 rotor airfoils. Therefore, an accurate calculation would require a minimum of 25 airfoils (11 in the stator row and 14 in the rotor row). In order to avoid the computational expense involved in simulating the flow associated with 25 airfoils, the rotor airfoil was enlarged by a factor of 28/22, keeping the pitch-to-chord ratio the same. It was then assumed that there were 22 airfoils in the rotor row. This assumption makes it possible to perform a calculation with only one rotor and one stator, thus reducing computation time by more than an order of magnitude. The second approximation was the assumption of two-dimensional flow in the midspan region. The results of Ref. 11 were then obtained by solving the thin-layer Navier-Stokes equations in two dimensions.

In the present study the approximation of two-dimensionality is removed, and three-dimensional airfoil geometries are used. In addition, the hub, outer casing, and rotor-tip clearance are all included in the calculation. A system of patched and overlaid grids is used to discretize the rather complex geometry of the three-dimensional configuration. An implicit, upwind third-order-accurate method is used in all the patches (the calculation of Ref. 11 used a hybrid upwind/central-difference scheme near the surface boundaries, for reasons mentioned later in the text). The equations solved are the unsteady, thin-layer Navier-Stokes equations in three dimensions, and the turbulence model is a modification of the Baldwin-Lomax model[13] that is developed in Ref. 14.

The following sections describe the grid-generation procedure, the integration method, and the various boundary conditions used, including the patch and overlay conditions. The computed results and comparisons of these results with experimental data are presented in a companion paper (Part II).

Grid System for the Rotor-Stator Configuration

A combination of patched and overlaid grids is used to discretize the regions surrounding the rotor-stator configuration. The region can be discretized using only patched grids. However, the number of zones required to solve the problem accurately would be twice as many as that required when both patched and overlaid grids are used in conjunction with each other. Overlaid-grid calculations are difficult to make conservative at the overlay boundaries. Since the current calculation is entirely subsonic and free of discontinuities (the maximum Mach number in the system is less than 0.35), physically meaningful solutions can be obtained even with the use of the nonconservative form of the equations. Therefore, nonconservative overlap boundary conditions can be expected to yield accurate solutions.

The airfoil geometry used in the current study is the same as that used in the experimental investigation of Ref. 6. The geometry consists of 22 stator airfoils and 28 rotor airfoils. An accurate simulation of this configuration would require at least 11 stator airfoils and 14 rotor airfoils, thus making the computation extremely expensive. Therefore, the rescaling strategy of Ref. 11 was used to reduce the number of airfoils to one stator and one rotor airfoil. This was done by enlarging the rotor by the factor 28/22 and then assuming that there were only 22 rotor airfoils. The pitch-to-chord ratio of the rotor was not changed during the enlargement process. Figure 2 is a perspective view of the rotor-stator combination showing the pressure side of the stator and the suction side of the rotor. The rotor in this figure has been enlarged by the factor 28/22. The outer casing has been removed to obtain the view shown in Fig. 2.

The multizone grid used to discretize the region consists of five zones. The three-dimensional grid consists of a sequence of two-dimensional grids that are stacked together in the radial direction (from hub to tip). Since the two-dimensional grids at each radial location are similar (except in the tip clearance area), only the grid at one radial location is considered. It consists of the five two-dimensional zones shown in Fig. 3. The first zone contains the stator and is discretized with an O-grid. The second zone contains the rotor and is also discretized with an O-grid. The grids in these two zones were generated using an elliptic grid generator of the type developed in Ref. 15. Both the zones lie on a cylinder of constant radius, the radius being measured from the center of the hub. The radial locations of the stacked two-dimensional grids are the same for the rotor and stator zones. This leads to two-dimensional interface boundaries and, thus, reduces interface logic by almost an order of magnitude. Although the actual grids used for the calculation are very dense near the airfoil surfaces (to resolve the viscous effects), for the purpose of clarity Fig. 3 shows grids in which the points are equispaced in the direction normal to the airfoil surfaces.

The grids for zones 3 and 4 were generated using an algebraic grid generator. Zone 3 contains the inner stator zone, and zone 4 contains the inner rotor zone. In fact, the inner boundary of zone 3 corresponds to the outer boundary of zone 1 and, similarly, the inner boundary of zone 4 corresponds to the outer boundary of zone 2. This positioning of the inner and outer stator zones (and the inner and outer rotor zones) facilitates information transfer between these zones. As in the case of the inner zones, the outer zones are also located at the same radial locations. The outer zones abut each other along the patch boundary ABCD and slip past each other as the rotor airfoil rotates. It is advantageous to use a patch boundary (as opposed to an area of overlay) where one system of grids moves relative to another system of grids because both time accuracy and conservation can be more easily controlled in patched-grid calculations.

An interesting feature of zones 3 and 4 as seen in Fig. 3 is that they do not align with each other. The segment AB of zone 4 does not seem to align with any part of the patch boundary of zone 3; similarly, the segment CD of zone 3 does not seem to align with any part of the patch boundary of zone 4. However, the periodicity boundary condition can be used to solve this problem, the result being that the segment AB is matched with the segment CD.

The rotor-tip clearance is about 0.4% of the span. Therefore, the volume corresponding to the last 0.4% of the span (or the first 0.4% of the span from the outer casing) does not contain the rotor airfoil. The stator, on the other hand, extends all the way from the hub to the outer casing and is attached at both ends. The grid system in the last 0.4% of the span is chosen to reflect the absence of the rotor airfoil. The rotor region is discretized using three grids: inner and outer rotor-type grids, and a grid that would have been interior to the rotor airfoil if that airfoil had been present.This interior grid is shown in Fig. 3 and is essentially an O-grid with the innermost O-grid line collapsing into a curve. The set of innermost O-grid lines form a surface along which the grid transformation is undefined and, therefore, requires special treatment during the solution process. The innermost rotor grid will be referred to as the interior rotor grid in the rest of the text. The rotor interior grids exist only in the the last 0.4% of the span. At lower radial locations the composite grid of Fig. 3 consists of only the first four zones.

As indicated before, grid points are densely packed close to the airfoil surfaces in zones 1 and 2 to resolve the viscous

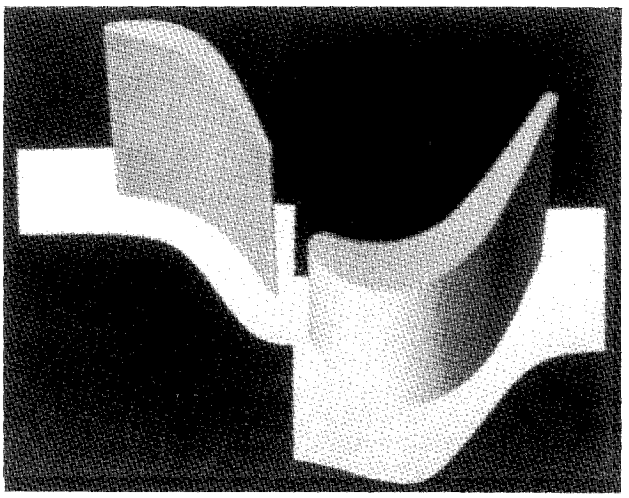

Fig. 2 Rotor-stator geometry of Ref. 6 (with enlarged rotor). A perspective view showing the pressure side of the stator and the suction side of the rotor.

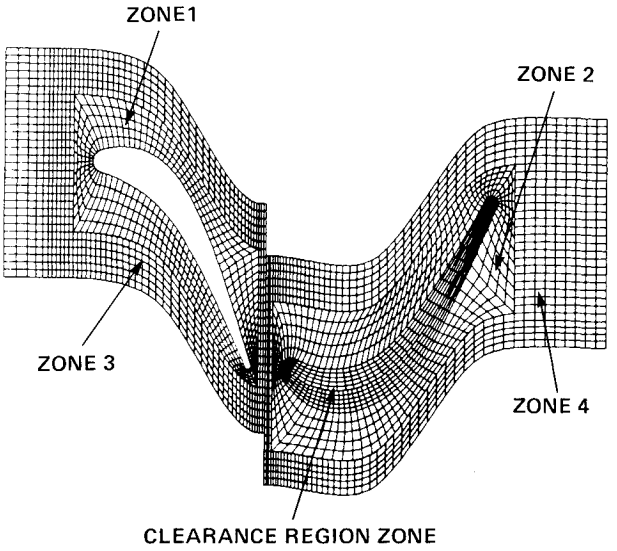

Fig. 3 Composite grid containing zones 1–5 at 100% span.

effects. Viscous effects are also predominant in the boundary layers associated with the hub and outer casing. The stacking of the two-dimensional grids in the radial direction reflects the presence of the these two boundary layers; the two-dimensional grids are packed densely near the hub and outer casing. At each radial location the inner grids contained 2121 points each (101×21), and the two outer grids contained 1798 (58×31) and 1860 (60×31) grid points, respectively. The interior rotor grid contained 1111 grid points (101×11). The composite three-dimensional grid consisted of 25 two-dimensional grids stacked together with the rotor-tip clearance area corresponding to the last five two-dimensional grids in the radial direction. The total number of grid points used for the calculation was 203,055.

Integration Method

The integration method used in all the zones is a third-order-accurate, iterative, implicit, upwind scheme. To describe the scheme, the unsteady Navier-Stokes equations in three spatial dimensions are considered:

$$\boldsymbol{Q}_t + \boldsymbol{E}_x + \boldsymbol{F}_y + \boldsymbol{G}_z = \boldsymbol{R}_x + \boldsymbol{S}_y + \boldsymbol{T}_z \tag{1}$$

where

$$\boldsymbol{Q} = \begin{bmatrix} \rho \\ \rho u \\ \rho v \\ \rho w \\ e \end{bmatrix} \quad \boldsymbol{E} = \begin{bmatrix} \rho u \\ p + \rho u^2 \\ \rho uv \\ \rho uw \\ (e+p)u \end{bmatrix} \quad \boldsymbol{F} = \begin{bmatrix} \rho v \\ \rho uv \\ p + \rho v^2 \\ \rho vw \\ (e+p)v \end{bmatrix} \quad \boldsymbol{G} = \begin{bmatrix} \rho w \\ \rho uw \\ \rho vw \\ p + \rho w^2 \\ (e+p)w \end{bmatrix} \tag{2a}$$

$$\boldsymbol{R} = \begin{bmatrix} 0 \\ \tau_{xx} \\ \tau_{xy} \\ \tau_{xz} \\ \beta_x \end{bmatrix} \quad \boldsymbol{S} = \begin{bmatrix} 0 \\ \tau_{yx} \\ \tau_{yy} \\ \tau_{yz} \\ \beta_y \end{bmatrix} \quad \boldsymbol{T} = \begin{bmatrix} 0 \\ \tau_{zx} \\ \tau_{zy} \\ \tau_{zz} \\ \beta_z \end{bmatrix} \tag{2b}$$

and where

$$\begin{gathered} \tau_{xx} = 2\mu u_x + \lambda(u_x + v_y + w_z) \\ \tau_{xy} = \mu(u_y + v_x) \quad \tau_{xz} = \mu(u_z + w_x) \\ \tau_{yx} = \tau_{xy} \quad \tau_{yy} = 2\mu v_y + \lambda(u_x + v_y + w_z) \\ \tau_{yz} = \mu(v_z + w_y) \quad \tau_{zx} = \tau_{xz} \quad \tau_{zy} = \tau_{yz} \\ \tau_{zz} = 2\mu w_z + \lambda(u_x + v_y + w_z) \\ \beta_x = u\tau_{xx} + v\tau_{xy} + w\tau_{xz} + \gamma\mu Pr^{-1}\bar{e}_x \\ \beta_y = u\tau_{yx} + v\tau_{yy} + w\tau_{yz} + \gamma\mu Pr^{-1}\bar{e}_y \\ \beta_z = u\tau_{zx} + v\tau_{zy} + w\tau_{zz} + \gamma\mu Pr^{-1}\bar{e}_z \\ \lambda = -2\mu/3 \quad \bar{e} = p/[\rho(\gamma - 1)] \end{gathered} \tag{3}$$

The independent variable transformation

$$\begin{gathered} \tau = t \quad \xi = \xi(x,y,z,t) \\ \eta = \eta(x,y,z,t) \quad \zeta = \zeta(x,y,z,t) \end{gathered} \tag{4}$$

is then applied to Eq. (1). For high-Reynolds-number flows with one of the coordinates in the transformed coordinate system (ξ,η,ζ) corresponding to the body surface, one usually makes the thin-layer assumption, i.e., the viscous terms evaluated as derivatives in the directions tangent to the body surface are assumed to be negligible in magnitude.[16] This concept was extended to thin layers in all three directions in Ref. 14. The viscous terms in any given coordinate direction contain only those terms that are derivatives in the same direction. The cross derivatives are neglected. A detailed discussion of this approach and its limitations can be found in Ref. 14. In the present study the thin-layer viscous terms are retained in two directions: in the direction normal to the hub surface (the ζ direction) and the direction normal to the airfoil surfaces (the η direction). The transformed equations now take the form

$$\bar{\boldsymbol{Q}}_\tau + \bar{\boldsymbol{E}}_\xi + \bar{\boldsymbol{F}}_\eta + \bar{\boldsymbol{G}}_\zeta = Re^{-1}(\bar{\boldsymbol{S}}_\eta + \bar{\boldsymbol{T}}_\zeta) \tag{5}$$

where

$$\begin{gathered} \bar{\boldsymbol{Q}} = \boldsymbol{Q}/J \\ \bar{\boldsymbol{E}}(\boldsymbol{Q},\xi) = (\xi_t\boldsymbol{Q} + \xi_x\boldsymbol{E} + \xi_y\boldsymbol{F} + \xi_z\boldsymbol{G})/J \\ \bar{\boldsymbol{F}}(\boldsymbol{Q},\eta) = (\eta_t\boldsymbol{Q} + \eta_x\boldsymbol{E} + \eta_y\boldsymbol{F} + \eta_z\boldsymbol{G})/J \\ \bar{\boldsymbol{G}}(\boldsymbol{Q},\zeta) = (\zeta_t\boldsymbol{Q} + \zeta_x\boldsymbol{E} + \zeta_y\boldsymbol{F} + \zeta_z\boldsymbol{G})/J \end{gathered} \tag{6}$$

The formulas for the metrics of the transformation $(\xi_t, \xi_x, \xi_y, \xi_z)$, $(\eta_t, \eta_x, \eta_y, \eta_z)$, and $(\zeta_t, \zeta_x, \zeta_y, \zeta_z)$ and the Jacobian of the transformation are given in Ref. 16. The vector $\bar{\boldsymbol{S}}$ is given by

$$\bar{\boldsymbol{S}} = \begin{bmatrix} 0 \\ K_1 u_\eta + K_2\eta_x \\ K_1 v_\eta + K_2\eta_y \\ K_1 w_\eta + K_2\eta_z \\ K_1[Pr^{-1}(\gamma-1)^{-1}(c^2)_\eta + (q^2/2)_\eta] + K_2K_3 \end{bmatrix} \tag{7}$$

where

$$\begin{gathered} K_1 = \mu(\eta_x^2 + \eta_y^2 + \eta_z^2) \\ K_2 = \mu(\eta_x u_\eta + \eta_y v_\eta + \eta_z w_\eta)/3 \\ K_3 = u\eta_x + v\eta_y + w\eta_z \\ q^2 = u^2 + v^2 + w^2 \end{gathered} \tag{8}$$

The vector $\bar{\boldsymbol{T}}$ can be obtained by replacing η with ζ in Eqs. (7) and (8).

Although the viscous terms in the η and ζ directions are included in the present formulation, the contribution from these terms can be negligible in a particular region if the grid resolution in this region is insufficient. For example, the $\bar{\boldsymbol{T}}$ term is negligible in regions away from the end walls because of the lack of sufficient grid resolution in the ζ direction in such regions. Similarly, the wake region is essentially calculated in an inviscid manner (although the airfoil boundary layers that give rise to the wake are computed accurately because of the high grid resolution in the direction normal to the airfoil). Computer speed and memory limitations preclude a more accurate treatment of the wake at the present time.

The factored, iterative, implicit algorithm is developed for the two-dimensional Euler equations in Ref. 17. The scheme as developed in Ref. 17 is second-order accurate in space and first-order accurate in time. The second-order accuracy in space results in a third-order fourth derivative in the truncation error. The constants multiplying the error term (for the second-order scheme presented in Ref. 17) are larger than those that multiply the fourth-derivative smoothing terms that are explicitly added to central-difference schemes. Hence, the second-order-accurate scheme of Ref. 17 may be too dissipative for viscous calculations (in viscously dominated regions). For this reason, Ref. 11 used a hybrid central-upwind difference scheme in the inner stator and rotor zones to simulate more accurately the viscously dominated regions.

Reference 18 presents a low-truncation-error second-order scheme and a third-order scheme that overcome this problem. These methods are used in conjunction with a relaxation approach in Ref. 18. In this study, the factored, iterative, third-

order-accurate scheme is presented. The scheme is given by

$$
\begin{aligned}
&[I + \frac{\Delta\tau}{\Delta\xi}(\nabla_\xi \tilde{A}^+_{i,j,k} + \Delta_\xi \tilde{A}^-_{i,j,k})]^p \\
&\times [I + \frac{\Delta\tau}{\Delta\eta}(\nabla_\eta \tilde{B}^+_{i,j,k} + \Delta_\eta \tilde{B}^-_{i,j,k} - Re^{-1}\delta_\eta \tilde{M})]^p \\
&\times [I + \frac{\Delta\tau}{\Delta\zeta}(\nabla_\zeta \tilde{C}^+_{i,j,k} + \Delta_\zeta \tilde{C}^-_{i,j,k} - Re^{-1}\delta_\zeta \tilde{N})]^p \times \\
&\times (\tilde{Q}^{p+1}_{i,j,k} - \tilde{Q}^p_{i,j,k}) = -\Delta\tau\Bigg(\frac{\tilde{Q}^p_{i,j,k} - \tilde{Q}^n_{i,j,k}}{\Delta\tau} \\
&+ \frac{\hat{E}^p_{i+\frac{1}{2},j,k} - \hat{E}^p_{i-\frac{1}{2},j,k}}{\Delta\xi} + \frac{\hat{F}^p_{i,j+\frac{1}{2},k} - \hat{F}^p_{i,j-\frac{1}{2},k}}{\Delta\eta} \\
&+ \frac{\hat{G}^p_{i,j,k+\frac{1}{2}} - \hat{G}^p_{i,j,k-\frac{1}{2}}}{\Delta\zeta} - \frac{\hat{S}^p_{i,j+\frac{1}{2},k} - \hat{S}^p_{i,j-\frac{1}{2},k}}{Re\Delta\eta} \\
&- \frac{\hat{T}^p_{i,j,k+\frac{1}{2}} - \hat{T}^p_{i,uj,k-\frac{1}{2}}}{Re\Delta\zeta}\Bigg)
\end{aligned}
\tag{9}
$$

where

$$
\tilde{A}^\pm = (\partial\tilde{E}/\partial\tilde{Q})^\pm \quad \tilde{B}^\pm = (\partial\tilde{F}/\partial\tilde{Q})^\pm \quad \tilde{C}^\pm = (\partial\tilde{G}/\partial\tilde{Q})^\pm
$$
$$
\tilde{M} = (\partial\tilde{S}/\partial\tilde{Q}) \quad \tilde{N} = (\partial\tilde{T}/\partial\tilde{Q}) \tag{10}
$$

and Δ, ∇, and δ are forward, backward, and central-difference operators, respectively. The quantities $\hat{E}_{i+\frac{1}{2},j,k}$, $\hat{F}_{i,j+\frac{1}{2},k}$, $\hat{G}_{i,j,k+\frac{1}{2}}$, $\hat{S}_{i,j+\frac{1}{2},k}$, and $\hat{T}_{i,j,k+\frac{1}{2}}$ are numerical fluxes consistent with the physical fluxes $\tilde{E}$, $\tilde{F}$, $\tilde{G}$, $\tilde{S}$, and $\tilde{T}$, respectively. In Eq. (9), $\tilde{Q}^p$ is an approximation to $\tilde{Q}^{n+1}$. When $p = 0$, $\tilde{Q}^p = \tilde{Q}^n$, and when Eq. (9) is iterated to convergence at a given time step, $\tilde{Q}^p = \tilde{Q}^{n+1}$. It should be noted that because the left-hand side of this equation can be driven to zero at each time step (by iterating to convergence), linearization and factorization errors can be driven to zero during the iteration process.

For problems in which only the asymptotic steady state is of interest, the iteration process need not be carried to convergence at each time step. In fact, when the number of iterations is restricted to one, the scheme reverts to a conventional, non-iterative implicit scheme of the type in Ref. 19. When second-order accuracy in time is required, the term $(\tilde{Q}^p_{i,j,k} - \tilde{Q}^n_{i,j,k})$ on the right-hand side of Eq. (9) must be replaced by $(1.5\tilde{Q}^p_{i,j,k} - 2.0\tilde{Q}^n_{i,j,k} + 0.5\tilde{Q}^{n-1}_{i,j,k})$ in addition to iterating to convergence. Typically, three to four iterations per time step are sufficient to reduce the residual by an order of magnitude or more.

The numerical fluxes $\hat{E}$, $\hat{F}$, and $\hat{G}$ can be evaluated in many different ways, the different choices leading to different schemes. The fluxes in this study were evaluated using Roe's scheme.[20] The numerical fluxes for the third-order scheme are evaluated as

$$
\begin{aligned}
\hat{E}_{i+\frac{1}{2},j,k} &= \tfrac{1}{2}[\tilde{E}(Q_{i,j,k}, \xi_{i+\frac{1}{2},j,k}) + \tilde{E}(Q_{i+1,j,k}, \xi_{i+\frac{1}{2},j,k})] \\
&+ 1/6[\Delta E^+(Q_{i-1,j,k}, Q_{i,j,k}, \xi_{i+\frac{1}{2},j,k}) \\
&- \Delta E^+(Q_{i,j,k}, Q_{i+1,j,k}, \xi_{i+\frac{1}{2},j,k}) \\
&+ 1/6[\Delta E^-(Q_{i,j,k}, Q_{i+1,j,k}, \xi_{i+\frac{1}{2},j,k}) \\
&- \Delta E^-(Q_{i+1,j,k}, Q_{i+2,j,k}, \xi_{i+\frac{1}{2},j,k})]
\end{aligned}
\tag{11}
$$

The flux differences $\Delta E^\pm$ using the method of Roe are given by

$$
\begin{aligned}
&\Delta E^\pm(Q_{i,j,k}, Q_{i+1,j,k}, \xi_{i+\frac{1}{2},j,k}) \\
&= \tilde{A}^\pm(Q_{i+\frac{1}{2},j,k}, \xi_{i+\frac{1}{2},j,k}) \times (Q_{i+1,j,k} - Q_{i,j,k})
\end{aligned}
\tag{12}
$$

The dependent variables necessary to evaluate $\tilde{A}^\pm$ at the intermediate point $(i + \frac{1}{2}, j, k)$ are evaluated from the following:

$$
\begin{aligned}
u_{i+\frac{1}{2}} &= \frac{u_i\sqrt{\rho_i} + u_{i+1}\sqrt{\rho_{i+1}}}{\sqrt{\rho_i} + \sqrt{\rho_{i+1}}} \\
v_{i+\frac{1}{2}} &= \frac{v_i\sqrt{\rho_i} + v_{i+1}\sqrt{\rho_{i+1}}}{\sqrt{\rho_i} + \sqrt{\rho_{i+1}}} \\
w_{i+\frac{1}{2}} &= \frac{w_i\sqrt{\rho_i} + w_{i+1}\sqrt{\rho_{i+1}}}{\sqrt{\rho_i} + \sqrt{\rho_{i+1}}} \\
h_{i+\frac{1}{2}} &= \frac{h_i\sqrt{\rho_i} + h_{i+1}\sqrt{\rho_{i+1}}}{\sqrt{\rho_i} + \sqrt{\rho_{i+1}}} \\
h &= \frac{e + p}{\rho}
\end{aligned}
\tag{13}
$$

The subscripts j and k have been left out of Eq. (13) for convenience. The eigenvalues of the Jacobian matrix $\tilde{A}$ need to be calculated in the process of calculating the matrices $\tilde{A}^\pm$. These eigenvalues are modified as outlined in Ref. 21 to prevent expansion shocks. The numerical fluxes $\hat{F}_{i,j+\frac{1}{2},k}$ and $\hat{G}_{i,j,k+\frac{1}{2}}$, are evaluated in a similar manner.

The viscous flux vector $\hat{S}_{i,j+\frac{1}{2},k}$ is evaluated using central differences, i.e.,

$$
\begin{aligned}
\hat{S}_{i,j+\frac{1}{2},k} &= \tilde{S}[Q_{i,j+\frac{1}{2},k}, (Q_\eta)_{i,j+\frac{1}{2},k}, \eta_{i,j+\frac{1}{2},k}] \\
Q_{i,j+\frac{1}{2},k} &\tfrac{1}{2}(Q_{i,j,k} + Q_{i+1,j,k}) \\
(Q_\eta)_{i,j+\frac{1}{2},k} &= Q_{i,j+1,k} - Q_{i,j,k}
\end{aligned}
\tag{14}
$$

The vector $\hat{T}_{i,j,k+\frac{1}{2}}$ is evaluated using similar expressions.

Boundary Conditions

The boundaries that contain the several grids that are used in this study can be broadly classified as natural boundaries and zonal boundaries. The natural boundaries include the stator inlet and the rotor exit; hub and outer casing surfaces; and the stator and rotor airfoil surfaces. The zonal boundaries comprise the various patch boundaries and overlay boundaries; for example, the patch boundary between the stator and rotor outer zones along which the relative motion of these two zones take place. Both the natural and zonal boundary conditions are discussed in this section.

Natural Boundary Conditions

The inner boundaries of the two O-grids correspond to the airfoil surfaces. Therefore, the no-slip boundary condition is enforced at all the points on these surfaces. Additionally, an adiabatic wall condition and a zero normal derivative of the pressure are also imposed on these surfaces. In the case of the rotor, the no-slip condition does not imply zero velocity; instead, it means that the fluid velocity at the rotor surface is equal to the rotor speed. The pressure derivative condition, the adiabatic wall condition, and the equation of state together yield

$$
\frac{\partial\rho}{\partial n} = 0
$$
$$
\frac{\partial e}{\partial n} = u\frac{\partial\rho u}{\partial n} + v\frac{\partial\rho v}{\partial n} + w\frac{\partial\rho w}{\partial n}
$$

where n is the direction normal to the blade surface. These boundary conditions are implemented in an implicit manner by using the following equation instead of Eq. (9) to update the grid points on the blade surfaces:

$$
C(\tilde{Q}^{p+1}_{i,1,k} - \tilde{Q}^p_{i,1,k}) + D(\tilde{Q}^{p+1}_{i,2,k} - Q^p_{i,2,k}) = 0 \tag{15}
$$

where

$$C = \begin{bmatrix} 1 & 0 & 0 & 0 & 0 \\ 0 & 1 & 0 & 0 & 0 \\ 0 & 0 & 1 & 0 & 0 \\ 0 & 0 & 0 & 1 & 0 \\ 0 & \alpha & \beta & \gamma & 1 \end{bmatrix} \quad D = \begin{bmatrix} \theta & 0 & 0 & 0 & 0 \\ 0 & 0 & 0 & 0 & 0 \\ 0 & 0 & 0 & 0 & 0 \\ 0 & 0 & 0 & 0 & 0 \\ 0 & \alpha\theta & \beta\theta & \gamma\theta & \theta \end{bmatrix}$$

$$\theta = -\frac{J_{i,2,k}}{J_{i,1,k}}$$

$$\alpha = -u_{\text{wall}}$$

$$\beta = -v_{\text{wall}}$$

$$\gamma = -w_{\text{wall}}$$

Equation (15) is an implicit, spatially first-order-accurate implementation of the no-slip (adiabatic wall) condition (first-order accurate because the zero normal derivative condition is implemented using a two-point forward difference). A second-order-accurate, three-point forward-difference corrector step is also implemented after each time step. It should be noted that Eq. (15) requires the grid to be orthogonal at the blade surfaces and the Jacobians of the transformation $J_{i,1,k}$ and $J_{i,2,k}$ to be independent of τ.

The no-slip boundary condition, the adiabatic wall condition, and the pressure derivative condition are also imposed on the hub and outer casing surfaces. The boundary condition on the outer casing is identical to the one used for the airfoil surfaces, except that the outer casing is a constant ζ surface (the airfoil surfaces are constant η surfaces). The hub, on the other hand, consists of two sections: the portion of the hub to which the stator airfoils are fixed is stationary, whereas the portion of the hub on which the rotor airfoils are mounted rotates along with the rotor airfoils. The two sections of the hub come together at the patch boundary that separates the outer stator and outer rotor grids. This presents a computational problem because the no-slip boundary condition implies a velocity discontinuity on that part of the patch boundary corresponding to the hub surface. The problem was overcome by imposing an average no-slip boundary condition along the set of grid points at the junction of the two hub sections.The average no-slip velocity was taken to be one-half the rotor speed.

The left boundary of the outer stator zone (zone 3) is a subsonic inlet boundary. Four quantities must be specified at this boundary. The four chosen for this study are a Riemann invariant, the entropy, and the radial and tangential flow velocities, i.e.,

$$R_1 = u + (2c/\gamma - 1)$$

$$s = (p/\rho^\gamma)$$

$$v_{\text{inlet}} = 0 \quad w_{\text{inlet}} = 0 \tag{16}$$

The fifth quantity (which is necessary to update the points on this boundary) is also a Riemann invariant:

$$R_2 = u - (2c/\gamma - 1) \tag{17}$$

and is extrapolated from the interior of zone 3. These conditions are appropriate for inviscid flow. In reality, the incoming flow contains two boundary layers: the hub boundary layer and the outer casing boundary layer. This problem was overcome by imposing the no-slip boundary condition only at those grid points of the hub and outer casing that were a small distance downstream of the inlet boundary (typically two grid points downstream of the inlet boundary), thus making the two boundary layers originate downstream of the inlet boundary. The above approximation is justified by the fact that the incoming boundary layers are extremely thin. However, this approximation was made only as a first step to three-dimensional rotor-stator calculations and will be replaced in the future by experimentally observed inlet distributions or by an additional zone that comprises the entrance to the stage.

The right boundary of the outer rotor zone (zone 4) is a subsonic exit boundary. In the absence of reverse flow (flow into the stage) in this area, only one quantity has to be specified at the exit boundary; the other four quantities can be extrapolated from the interior of zone 4. The quantity to be specified can be picked either to reflect all pressure waves as in the case of an open-end duct, or to transmit all pressure waves, as in the case of open-end duct, or to transmit all pressure waves, as in the case of an infinite duct. A detailed description of these two approaches for two-dimensional problems can be found in Ref. 7. For the purpose of pressure data comparison with the experimental results of Ref. 6, the pressure-reflection boundary condition was chosen.

In two dimensions, the pressure-reflection condition implies specifying a constant pressure at the rotor exit. In the three-dimensional case of this study, a constant pressure is imposed at midspan. The pressure at all other radial locations at the rotor exit are obtained from the radial equilibrium condition:

$$\frac{\partial p}{\partial r} = \frac{\rho v_t^2}{r} \tag{18}$$

where v_t is the tangential velocity and r the radius measured from the center of the hub. All five dependent variables are extrapolated implicitly from the interior of zone 4, using instead of Eq. (9) the equation

$$(\tilde{Q}^{p+1}_{i\max,j,k} - \tilde{Q}^{p}_{i\max,j,k}) - \frac{J_{i\max-1,j,k}}{J_{i\max,j,k}}(\tilde{Q}^{p+1}_{i\max} - \tilde{Q}^{p}_{i\max-1,j,k},) = 0 \tag{19}$$

A postupdate correction is then made to the pressure, using Eq. (18).

The calculation assumes that there are an equal number of rotor and stator airfoils in the stage. Hence, a simple periodicity boundary condition is employed on the constant η boundaries of the outer stator and rotor zones. The implicit implementation of this boundary condition is straightforward.

Zonal Boundary Conditions

There are several zonal boundaries that are used in the present calculation. These boundaries serve to separate the various zones. The requirements that zonal boundary conditions must meet before they can be used effectively have been outlined earlier. The various zonal boundary calculations can be made conservative (both overlap and patch conditions). However, since the flow in the entire region is in the low subsonic regime, flow discontinuities such as shocks and slip surfaces do not exist for the flow conditions of interest. Physically meaningful solutions to discontinuity-free flows can be obtained with the nonconservation form of the Euler and Navier-Stokes equations. Therefore, in the interest of simplicity, the various zonal boundary calculations were not made conservative. The zonal boundary conditions in the current computer program may have to be modified for transonic and supersonic flow conditions with the associated flow discontinuities.

The zonal boundaries used in the present calculation are:

1) The patch-overlap boundary between the inner and outer zones for the rotor and stator. Although Fig. 3 shows this boundary to be a patch boundary, the grid of the outer zone exists concurrently with the grid of the inner zone in the inner zone area. Information transfer from the inner zone to the outer zone takes place within the inner zone.

2) The patch boundary between the outer stator zone and the outer rotor zone. A one-grid-point overlap exists at this boundary, i.e., the outer stator zone penetrates the outer rotor zone to the extent of one grid point (in the direction of the axis of the hub) and vice versa.

3) The patch boundary between the interior rotor grid and the inner rotor grid. There is a one-to-one correspondence between the grid lines of these two grids where they meet and, hence, there is at most only a metric discontinuity along this patch boundary.

All of the zonal boundaries are treated in the following manner. The zonal boundary points are integrated by using the equation

$$(\tilde{Q}^{p+1} - \tilde{Q}^{p})_{z.b} = 0 \tag{20}$$

where z.b refers to the points on a zonal boundary. This is followed by an explicit, corrective interpolation procedure at the end of each iteration wherein the values of Q^{p+1} along the zonal boundary are obtained from interpolating the dependent variables of the neighboring grid in which the zonal boundary lies. For the inner boundaries of the outer grids, z.b. refers to the first set of points of the outer grids that lie within the corresponding inner grids. In the case of the outer boundaries of the inner grids, z.b. refers to the patch-boundary points seen in Fig. 3. For the patch boundary between the outer stator and rotor grids, z.b. refers to those points that form the extension of these grids into each other (the extensions are as described earlier).

Equation (20) has the property of decoupling the calculations in the different grids. A second iteration [Eq. (9)] for grid points in the vicinity of the zonal boundary is a must for stabilizing the scheme. It is important to note that Eq. (20) is not the same as that given by the following equation:

$$(\tilde{Q}^{n+1} - \tilde{Q}^{n})_{z.b} = 0 \tag{21}$$

Equation (20) [in addition to Eq. (9) in the interiors of zones] together with the postupdate correction mentioned above allows $(\tilde{Q}^{n+1} - \tilde{Q}^{n})_{z.b}$ to assume its right value when the iteration process is carried to convergence. Both time accuracy and a spatial accuracy consistent with the order of the interpolation scheme are maintained at the zonal boundaries by using Eq. (20).

The solution procedure can now be summarized in the following three steps:

1) Integrate the dependent variables at all the grid points of all the zones using Eq. (9) in conjunction with the implicit boundary conditions, both natural and zonal (only one iteration).

2) Perform the postupdate corrections to the dependent variables at the zonal boundary points of all zones as described above.

3) If the maximum value of the magnitudes of all $(\tilde{Q}^{p+1} - Q^{p})$ is less than a prescribed tolerance limit, go to the next integration step; if not, go back to step 1 and iterate.

Additional details regarding the implementation of zonal boundary conditions can be found in Refs. 8-10.

Summary

An unsteady, thin-layer Navier-Stokes code to study three-dimensional rotor-stator interaction problems has been developed. The hub, outer casing, and rotor-tip clearance are all an integral part of the code. With minor modifications the code can be used for a variety of geometries, for example, geometries with clearances at both ends or no clearances at all. The code uses patched and overlaid grids that move relative to each other to be able to simulate the motion of the rotor airfoils with respect to the stator airfoils. The code was used to simulate subsonic flow past a turbine stage for which considerable data exist.

The code uses a third-order-accurate upwind scheme to integrate the unsteady, thin-layer Navier-Stokes equations. The scheme is set in an iterative, implicit framework such that factorization and linearization errors can be driven to zero at each time step. The integration scheme, the natural boundary conditions of the problem, and the zonal boundary conditions are all discussed in the paper. The computed results for the turbine geometry presented in this paper and a comparison of these results with experimental data may be found in the companion paper (Part II).

References

[1]Delaney, R. A., "Time-Marching Analysis of Steady Transonic Flow in Turbomachinery Cascades Using the Hopscotch Method," *Journal of Engineering for Power,* Vol. 105, April 1983, pp. 272-279.

[2]Davis, R. L., Ni, R.-H., and Carter, J. E., "Cascade Viscous Flow Analysis Using the Navier-Stokes Equations," AIAA Paper 86-0033, Jan. 1986.

[3]Subramanian, S. V., Bozzola, R., and Povinelli, L. A., "Computation of Three-Dimensional, Rotational Flow through Turbomachinery Blade Rows for Improved Aerodynamic Design Studies," American Society of Mechanical Engineers, Paper 86-GT-26, June 1986.

[4]Chima, R. V., "Development of an Explicit Multigrid Algorithm for Quasi-Three-Dimensional Viscous Flows in Turbomachinery," NASA TM-87128, 1986.

[5]Weinberg, B. C., Yang, R. J., McDonald, H., and Shamroth, S. J., "Calculations of Two- and Three-Dimensional Transonic Cascade Flow Fields Using the Navier-Stokes Equations," *Journal of Engineering for Gas Turbines and Power,* Vol. 108, Jan. 1986, pp. 93-102.

[6]Dring, R. P., Joslyn, H. D., Hardin, L. W., and Wagner, J. H., "Turbine Rotor-Stator Interaction." *Journal of Engineering for Power,* Vol. 104, Oct.1982, pp. 729-742.

[7]Erdos, J. I., Alzner, E., and McNally, W., "Numerical Solution of Periodic Transonic Flow through a Fan Stage," *AIAA Journal,* Vol. 15, Nov. 1977, pp. 1559-1568.

[8]Rai, M. M., "A Conservative Treatment of Zonal Boundaries for Euler Equation Calculations," *Journal of Computational Physics,* Vol. 62, Feb. 1986, pp. 472-503.

[9]Rai, M. M., "An Implicit Conservative Zonal Boundary Scheme for Euler Equation Calculations," *Computers and Fluids,* Vol. 14, No. 3, 1986, pp. 295-319.

[10]Rai, M. M., "A Relaxation Approach to Patched-Grid Calculations with the Euler Equations," *Journal of Computational Physics,* Vol. 66, Sept. 1986, pp. 99-131.

[11]Rai, M. M., "Navier-Stokes Simulations of Rotor-Stator Interaction Using Patched and Overlaid Grids,"*Journal of Propulsion and Power,* Vol. 3, Sept.-Oct. 1987, pp. 387-396.

[12]Gibeling, H. J., Weinberg, B. C., Shamroth, S. J., and McDonald, H., "Flow through a Compressor Stage," Scientific Research Associates, Glastonbury, CT, Rept. R86-910004-F, May 1986.

[13]Baldwin, B. S. and Lomax, H., "Thin Layer Approximation and Algebraic Model for Separated Turbulent Flow," AIAA Paper 78-0257, Jan. 1978.

[14]Hung, C. M. and Buning, P. G., "Simulation of Blunt-Fin-Induced Shock-Wave and Turbulent-Layer Interaction," *Journal of Fluid Mechanics,* Vol. 154, May 1985, pp. 163-185.

[15]Steger, J. L. and Sorenson, R. L., "Automatic Mesh-Point Clustering near a Boundary in Grid Generation with Elliptic Partial Differential Equations," *Journal of Computational Physics,* Vol. 33, Dec. 1979, pp. 405-410.

[16]Pulliam, T. H. and Steger, J. L., "On Implicit Finite-Difference Simulations of Three-Dimensional Compressible Flow," *AIAA Journal,* Vol. 18, Feb. 1980, pp. 159-167.

[17]Rai, M. M. and Chakravarthy, S. R., "An Implicit Form for the Osher Upwind Scheme," *AIAA Journal,* Vol. 24, May 1986, pp. 735-743.

[18]Chakravarthy, S. R., Szema, K.Y., Goldberg, U. C., and Gorski, J. J., "Application of a New Class of High-Accuracy TVD Schemes to the Navier-Stokes Equations," AIAA Paper 85-0165, Jan. 1985.

[19]Beam, R. M. and Warming, R. F., "An Implicit Factored Scheme for the Compressible Navier-Stokes Equations," *Proceedings of the AIAA 3rd Computational Fluid Dynamics Conference,* AIAA, New York, 1977 pp. 130-140.

[20]Roe, P. L., "Approximate Riemann Solvers, Parameter Vectors, and Difference Schemes," *Journal of Computational Physics,* Vol. 43, Oct. 1981, pp. 357-372.

[21]Yee, H. C., Warming, R. F., and Harten, A., "Implicit Total Variation Diminishing (TVD) Schemes for Steady-State Calculations," NASA TM-84342, 1983.

Three-Dimensional Navier-Stokes Simulations of Turbine Rotor-Stator Interaction; Part II – Results

Man Mohan Rai*
NASA Ames Research Center, Moffett Field, California

Fluid flows within turbomachinery tend to be extremely complex. Understanding such flows is crucial to efforts to improve current turbomachinery designs, and the computational approach can be used to great advantage in this regard. This study presents a finite-difference, unsteady, thin-layer Navier-Stokes solution to the flow within an axial turbine stage. The computational methodology developed for this simulation is presented in Part I of this paper. The calculation includes end-wall and tip-leakage effects. Results in the form of time-averaged surface pressures, pressure amplitudes (corresponding to the pressure fluctuation in time), near-surface velocity vectors, and pressure contours in the passage areas are presented. The numerical results are compared with experimental data wherever possible and the agreement between the two is found to be good.

Introduction

An accurate numerical analysis of the flows associated with rotor-stator configurations can be very helpful in optimizing the performance of turbomachinery. However, such analyses tend to be computationally expensive and extremely complex because 1) the flow is inherently unsteady, 2) the geometries involved are complicated, 3) the flow periodically transitions between laminar and turbulent flow, and 4) there is relative motion between the stator and rotor rows. Nevertheless, a clear understanding of the aerodynamic process associated with turbomachinery can aid the design process considerably.

Several calculations of cascade flow have already been reported in the literature. These studies include two- and three-dimensional calculations using both the Euler and Navier-Stokes equations. Although analyses of flows through isolated rows can be used to study many of the fluid mechanical phenomena in turbomachinery, such analyses yield no information regarding the unsteadiness arising out of the interaction of moving and stationary rows of airfoils. These interaction effects become increasingly important as the distance between successive rows is decreased. The experimental results of Ref. 1 show that the temporal pressure fluctuation near the leading edge of the rotor can be as much as 72% of the exit dynamic pressure when the axial gap is reduced to 15% of the chord length (for the operating conditions and geometry chosen). Thus, the need for treating the rotor and stator airfoils as a system when interaction effects are predominant is obvious.

In this study the unsteady, three-dimensional, thin-layer, Navier-Stokes rotor-stator code developed in Part I of this paper was used to simulate subsonic flow past a turbine stage for which considerable experimental data exist.[1] Hub-to-tip variations of time-averaged pressure and pressure amplitudes (corresponding to the temporal fluctuation of pressure) and velocity fields to show the various vortical structures (horseshoe vortices at the hub and tip for the stator and rotor) are included. The numerically obtained predictions are compared with the experimental data of Ref. 1. These comparisons include time-averaged pressures, pressure amplitudes, and limiting streamlines on the rotor and stator surfaces.

Presented as Paper 87-2058 at AIAA/SAE/ASME/ASEE 23rd Joint Propulsion Conference, San Diego, California, June 29-July 2, 1987; received Dec. 8, 1987; revision received June 22, 1988. This paper is declared a work of the U.S. Government and therefore is in the public domain.

*Research Scientist. Associate Fellow AIAA.

Results

In this section, results obtained for the rotor-stator configuration shown in Fig. 1 are presented. These results were obtained by integrating the governing equations and the boundary conditions as described in Part I of this paper. Three iterations were performed at each step. Approximately five cycles [a cycle corresponds to the motion of the rotor through an angle equal to $(2\pi/N)$rad, where N is the number of stator or rotor airfoils] were required to eliminate the initial transients and establish a solution that was periodic in time. The calculation was performed at a constant time-step value of about 0.04. (This translates into 2000 time steps/cycle.)

The dependent variables are nondimensionalized with respect to the inlet pressure (p_∞) and density (ρ_∞). This yields $u_\infty = M_\infty\sqrt{\gamma}$, $v_\infty = 0$, and $\omega_\infty = 0$ (inlet flow is axial), where M_∞ is the inlet Mach number. The inlet Mach number used for this calculation was 0.07. The Riemann invariants that are prescribed at the inlet are determined using the dependent variables defined above. The rotor velocity is determined from the desired flow coefficient (0.78 in this case) and the inlet axial velocity (u_∞). Since the quantities that are prescribed at the inlet boundary are the Riemann invariants and not the dependent variables themselves, the values of u, v, w, ρ, and p obtained at the inlet, when the solution becomes periodic in time, are different from those used to determine the Riemann invariants. Hence, the rotor velocity needs to be recomputed and the calculation needs to be continued for a few more

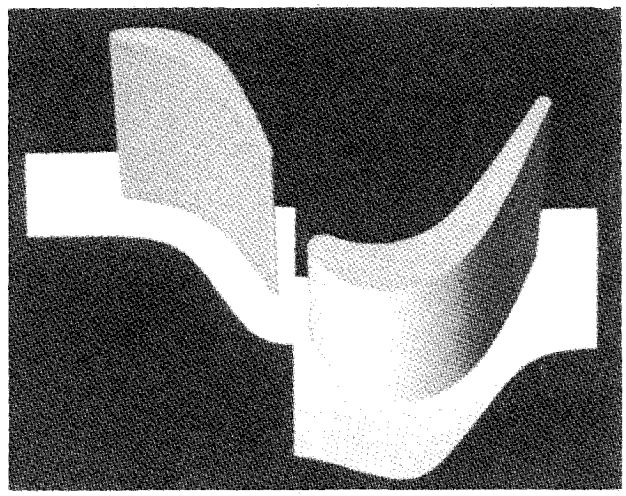

Fig. 1 Rotor-stator geometry.[1]

cycles (which then establishes a slightly different time-periodic solution). This iterative process must be continued until the calculated flow coefficient is equal to the required flow coefficient within certain limits of tolerance. The iterative process was not carried out for the three-dimensional calculation presented in this study because the right value of the rotor velocity (to obtain a flow coefficient of 0.78) was known a priori from the two-dimensional calculation of Ref. 2.

The Reynolds number used for this calculation was 100,000/in. This value of the Reynolds number is close to the experimental value but not exactly so; the differences between experiment and theory are discussed later in the text. A modified version of the Baldwin-Lomax model[3,4] was used to determine the eddy viscosity; the kinematic viscosity was calculated using Sutherland's law.

In the figures that follow, several comparisons are made with experimental data. The following points must be kept in mind when evaluating these comparisons:

1) The airfoil geometry used in the numerical calculation only approximates that used in the experiment. The actual configuration consisted of 22 stator airfoils and 28 rotor airfoils. However, the calculation was performed with 22 of each with an enlarged rotor geometry. In addition, because the rotor airfoil was enlarged only in two directions (not in the spanwise direction), the aspect ratio of the rotor airfoil used in the calculation is smaller than the actual aspect ratio.

2) The enlargement of the rotor, together with the use of the experimental value of the Reynolds number (100,000/in.), results in a larger Reynolds number for the number for the rotor (larger by a factor of 28/22). The rescaling of the rotor geometry requires the modification of the Reynolds number to simulate equivalent conditions in the calculation. It is not clear how this modification should be effected.

3) The axial gap between the airfoils in the experiment was 15% of the chord length. It is difficult to estimate the equivalent axial gap in the case of the modified rotor. The calculation was performed using an axial gap that was 15% of the average chord length.

4) The tip clearance in the experiment was 1.4% of the span, whereas the tip clearance used in the present calculation was 0.4% of the span. A preliminary calculation with a clearance of 1.4% resulted in separated flow on the suction side of the rotor in the last 40% of the chord in the vicinity of the clearance region. Experience indicates that the Baldwin-Lomax turbulence model does not predict eddy viscosities accurately in separated regions. For this reason, the clearance was reduced until the flow reattached. Accurate calculations for large clearance cases will require a turbulence model that performs well in separated regions.

Hub-to-Tip Variations of Time-Averaged Pressures

Figures 2a–2c and 3a–3c show time-averaged stator and rotor surface pressure distributions. The experimental data presented in these figures were obtained with an axial gap of 50%,[5] whereas the numerical data were obtained with an axial gap of 15%. However, the results of Ref. 1 indicate that the axial gap has negligible effect on time-averaged stator surface pressures and, at most, a weak effect on time-averaged rotor surface pressures. Hence, the following comparisons between theory and experiment, to a large extent, do indicate the performance of the present computational approach (subject to the geometrical and other approximations discussed earlier).

Figures 2a–2c show experimental and numerical time-averaged pressure coefficients C_p on the stator at 2.0, 50.0, and 98.0% of the span, respectively (these pressure values are plotted as a function of the axial distance along the stator). The pressure coefficient is defined as

$$C_p = \frac{p_{avg} - (p_t)_{inlet}}{1/2\rho_{inlet}\omega^2}$$

where p_{avg} is the static pressure averaged over one cycle,

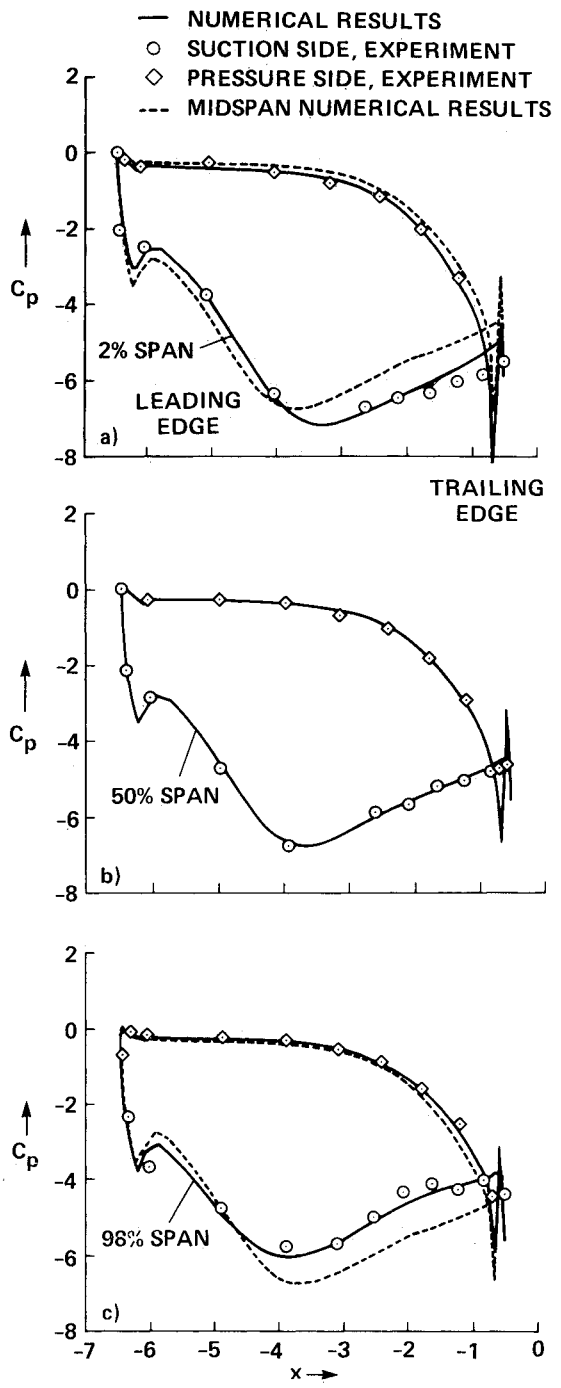

Fig. 2 Spanwise variation of time-averaged pressure distributions on the stator: a) 2.0% span; b) 50.0% span; c) 98.0% span.

$(p_t)_{inlet}$ and ρ_{inlet} are the average total pressure and density, respectively, at midspan at the inlet, and ω is the velocity of the rotor at midspan. The dashed lines in all these figures represent the numerical results at midspan. The midspan data is provided to enable comparisons and to show the changes in stator loads from hub to tip.

The comparison between theory and experiment is good all the way from the hub to the tip. A small separation bubble was found on the trailing edge circle of the stator in the numerical results. This is seen as a spatial fluctuation in pressure toward the trailing edge of the stator. The computed two-dimensional results of Ref. 2 are almost identical to the three-dimensional results presented here.

Figures 3a–3c show the time averaged C_p distributions on the rotor airfoil at 2.0, 50.0, and 87.5% of the span, respectively. The dashed lines on these figures once again

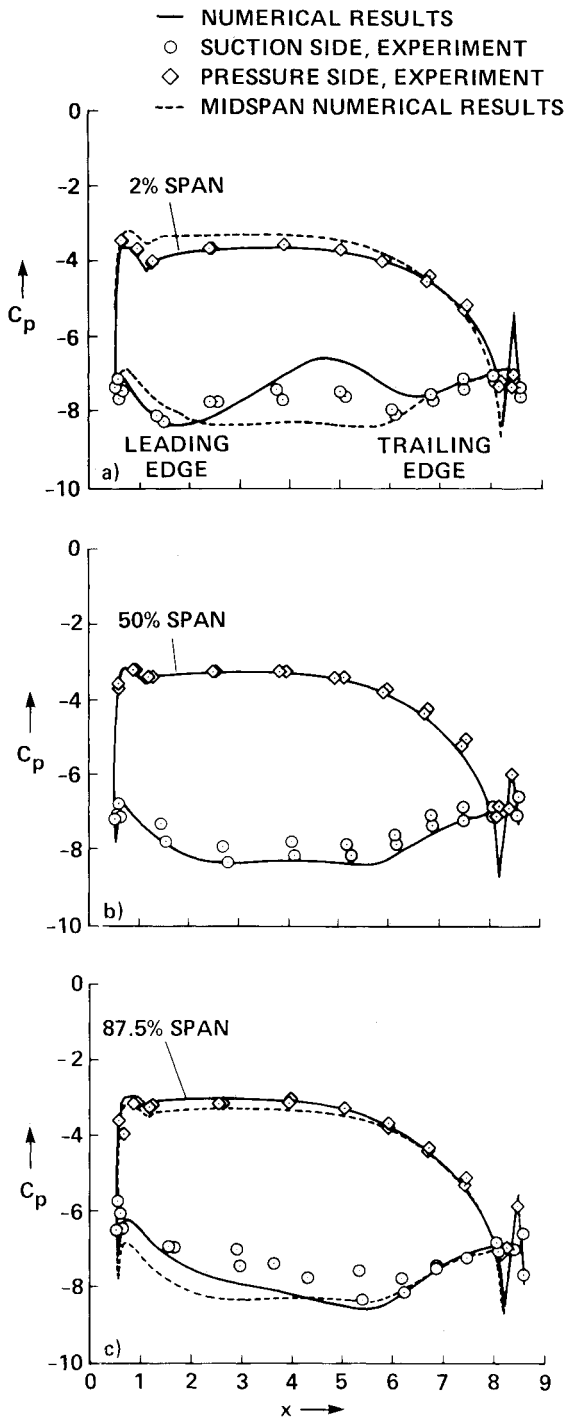

Fig. 3 Spanwise variation of time-averaged pressure distributions on the rotor: a) 2.0% span; b) 50.0% span; c) 87.5% span.

represent the numerical data at midspan. Figures 3a–3c show a reasonably good agreement between theory and experiment. The numerical results lie close to the range of experimental data, except at the hub. The suction side of the rotor airfoil in the region of the hub shows larger calculated values of pressure than found experimentally. It is not yet clear whether the geometrical approximations made to obtain the calculated values of pressure or an accuracy problem, or an experimental uncertainty causes this difference between theory and experiment. However, on the pressure side of the airfoil, an excellent agreement between the experimental and numerical data is obtained from hub to 87.5% of the span. Comparisons at larger values of the span cannot be expected to be good because the tip-leakage vortex in the experiment is much stronger than the one found in the calculation. (This is because of the larger clearance between the rotor and the casing in the experiment.)

As in the case of the stator, a small separation bubble was found on the trailing edge circle of the rotor. The bubble is seen as a sharp dip and rise in the pressure curves of Figs. 3a–3c. Unlike the stator C_p distribution, the three-dimensional calculation yields midspan time-averaged pressures that are better than the two-dimensional results of Ref. 2. The two-dimensional suction side pressure was lower than the experimental value by about 5% in the region ($5.0 \leq x \leq 6.0$). The three-dimensional calculation shows a smaller mismatch between theory and experiment.

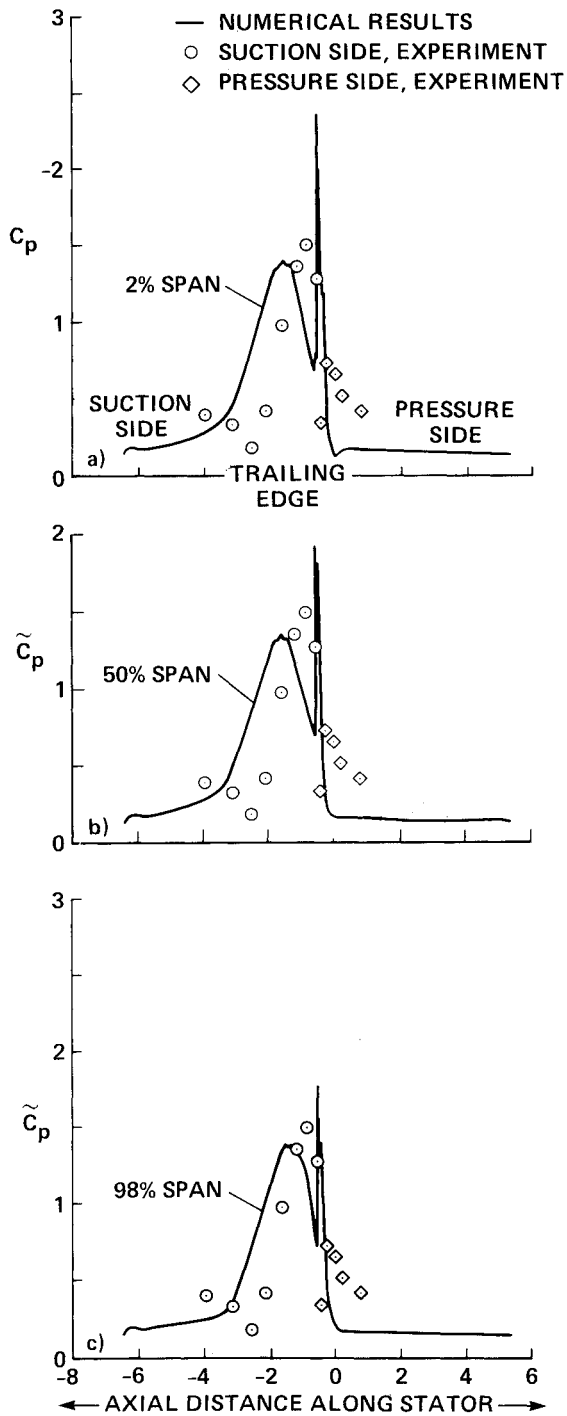

Fig. 4 Spanwise variation of pressure-amplitude distributions on the stator: a) 2.0% span; b) 50.0% span; c) 98.0% span.

Hub-to-Tip Variations of Pressure Amplitudes

The amplitude of the temporal pressure fluctuation is a measure of the unsteadiness of the flow. Figures 4a–4c show pressure amplitudes $\tilde{C}_p$ on the surface of the stator plotted as a function of the axial distance. The quantity $\tilde{C}_p$ is defined as

$$\tilde{C}_p = \frac{p_{\max} - p_{\min}}{1/2\rho_{\text{inlet}}\omega^2}$$

where $p_{\max}$ and $p_{\min}$ are the maximum and minimum pressures that occur over a cycle at a given point. The symbols in all of these figures represent the midspan experimental values of Ref. 1. In general, all the curves are very similar to each other and to the midspan experimental values.

The agreement between experiment and theory at midspan is fairly good. The numerical data seem to form a wider large amplitude region than that found experimentally. In addition, the predicted peak is to the left of the experimental peak. These distortions are because of a combination of reasons discussed in the following.

The current calculation uses an equal number of stator and rotor airfoils. A simple acoustic analysis tells us that in such a situation every harmonic in time (if one were to perform a Fourier decomposition of the unsteady pressures in the region between the stator and rotor) results in a propagating wave in the axial direction. In the experimental configuration there are 22 stator airfoils and 28 rotor airfoils. This results in only the higher harmonics in time giving rise to propagating waves; the lower harmonics give rise to decaying signals. Since the higher harmonics are much smaller in magnitude, the unsteady pressure that reach the exit boundary are much smaller in the case of the experiment. The reflective exit boundary condition used in the calculation reflects the relatively large calculated pressure waves that reach the exit boundary back into the system, thus distorting the unsteady pressures everywhere in the system.

The problem can be cured only to a limited extent by developing a nonreflective boundary condition. This is because the far-field pressure signals being generated by the one-rotor/one-stator system are different from those that would be generated by a multirotor/multistator system. The right approach is to perform a multirotor/multistator calculation (the reflective properties of the exit boundary condition will be relatively less important for more realistic rotor and stator airfoil counts). Such a calculation for the two-dimensional case, with additional details on the importance of exit boundary conditions, is presented in Ref. 6. The multiple airfoil results of Ref. 6 show a considerable improvement over the one-rotor/one-stator results. Current computer speed and memory limitations make a multirotor/multistator calculation in three spatial dimensions extremely expensive.

Figures 5a–5c show pressure amplitudes on the rotor at 2.0, 50.0, and 98.0% span, respectively. The symbols in these figures once again represent experimental values at midspan. Unlike the stator pressure amplitudes, the rotor pressure amplitudes change considerably as we move from hub to tip. The leading edge peak first increases and then decreases in the spanwise direction. The suction side peak continually decreases from hub to tip. However, the pressure side amplitudes on the rotor remain almost the same from hub to tip.

The agreement between theory and experiment at midspan is not as good as in the case of the stator. The suction side amplitude peak is shifted to the left of the experimental one. A sizable portion of the pressure side peak toward the trailing edge is due to strong pressure waves being reflected back from the exit boundary. The stator pressure amplitude distributions tend to be predicted better because the rotor airfoils shield the stator airfoils from the reflected pressure waves (reflected off the exit boundary). The numerical $\tilde{C}_p$ distribution of Fig. 5b is in agreement with the two-dimensional, one-rotor/one-stator calculations in Ref. 6 that are obtained with a reflective exit boundary condition. The numerical data shown in Fig. 5b do predict all the qualitative features shown by the experiment.

Instantaneous Pressures in the Stator and Rotor Passages

Figure 6 shows pressure contours at the hub at a particular instant in time. Although the calculation was performed with only two airfoils, for the sake of clarity this contour plot depicts several airfoils. The information regarding the additional airfoils is obtained from the periodicity condition. The figure shows small-amplitude, high-frequency oscillations superimposed on the contours. These oscillations are caused by the decoupling of the continuity, momentum, and energy equations that occur at low Mach numbers and will disappear for calculations at higher Mach numbers. One interesting feature is that the suction side pressure minimum on the hub

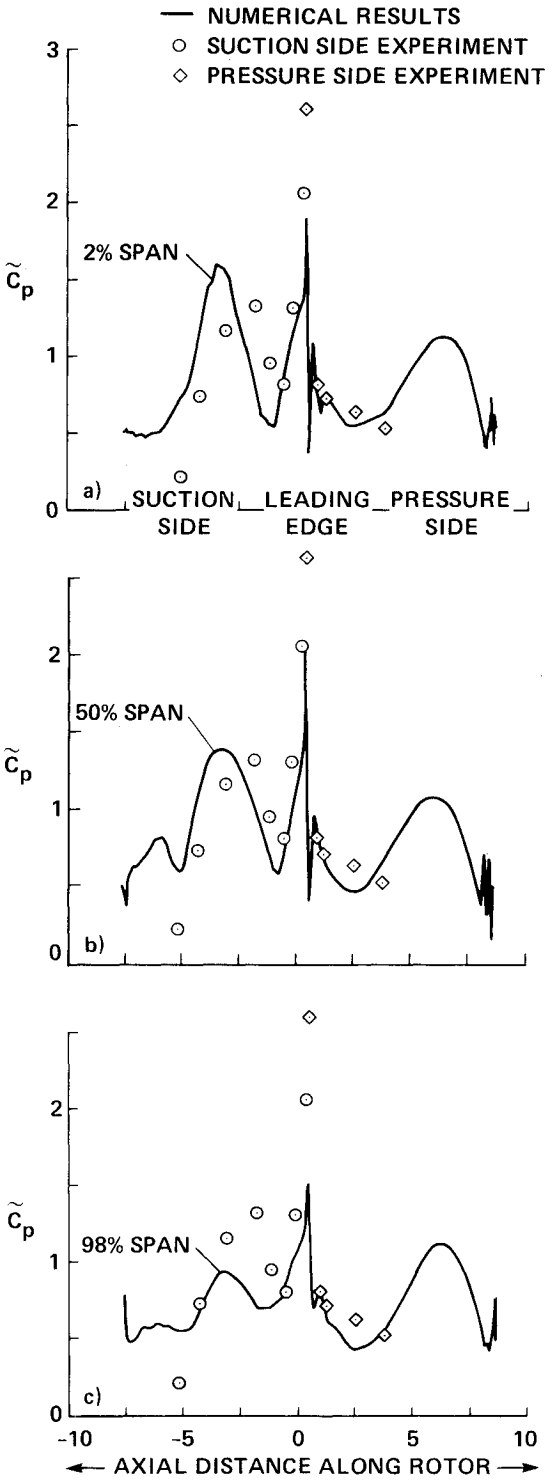

Fig. 5 Spanwise variation of pressure-amplitude distributions on the rotor: a) 2.0% span; b) 50.0% span; c) 98.0% span.

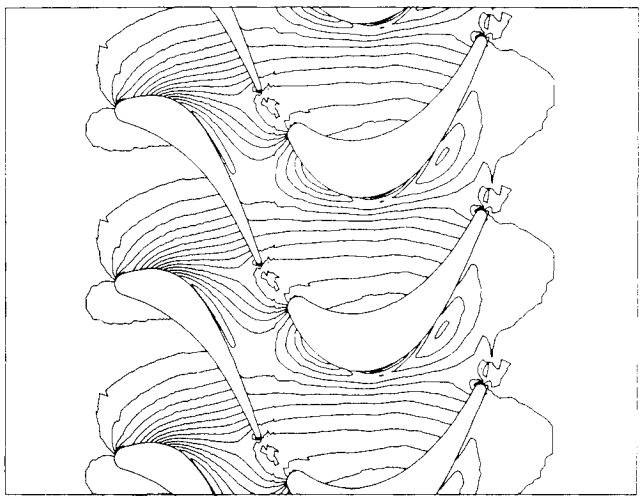

Fig. 6 Instantaneous pressure contours at the hub.

in the stator row does not occur on the stator airfoil. Instead, it has moved into the channel. This feature has been observed experimentally in Ref. 7. A similar phenomenon also occurs on the rotor hub; in fact, this effect is more pronounced in the rotor row.

Time-Averaged Limiting Streamlines and Near-Surface Velocities

The nature of the flow close to the surfaces of the rotor and stator airfoils and the hub surface can be better understood from the pattern of limiting streamlines on these surfaces and from velocity vectors near these surfaces (one grid point away from the surface). These streamline patterns not only yield information regarding the flow close to the surface, but also reflect the presence of fluid mechanical entities such as shocks and vortices in the interior of the region under consideration. The following results presented were obtained by releasing particles on the grid surface just above the hub or airfoil surface and then allowing those particles to move according to the time-averaged velocity field. The motion of the particles is restricted to the grid surface on which they were originally released (the out-of-surface component of velocity is not used to move the particle). The velocity vectors in the following figures have all been normalized and, hence, do not represent the actual velocity magnitudes but only the local flow direction.

Figure 7 shows limiting streamlines on the stator-hub surface. The flow is uniformly axial in the inlet region and then aligns itself to the stator passage as it moves through the passage. The details of the flow in the leading-edge region are also seen in Fig. 7. The stator and stator hub, together, are topologically similar to a blunt fin mounted on a flat surface. The flow separates as it approaches the leading edge of the stator. This flow separation results in the formation of a horseshoe vortex, one leg of which wraps itself around the leading edge of the stator and then impinges on the suction side at about 35% of the chord. The other leg of the vortex enters the passage and impinges on the suction side of the next stator. This leg of the vortex will be referred to as the passage vortex in the rest of the text. Figure 7 also shows a saddle point of separation with two attachment lines and two separation lines. The first attachment line starts at the saddle point and meets the airfoil surface on the leading-edge circle on the pressure side of the stator. The second attachment line starts at the saddle point and extends upstream toward the inlet boundary. The separation lines extend from the saddle point into adjacent passages. The horseshoe vortex is formed between the separation lines and the airfoil surface. The results of Fig. 7 agree qualitatively with the experimental results of Ref. 7 (obtained for a cascade geometry).

Figure 8 shows limiting streamlines on the suction side of the stator. The upward motion of the fluid particles near the hub is caused by the passage vortex generated by the neighboring stator airfoil. The upward motion is confined to the first 15% of the span. This effect is a result of the passage vortex being drawn toward the hub (the fluid in the passage vortex is of lower total pressure and is, therefore, drawn toward a lower radial location). Figure 8 also indicates the line of separation that delineates the largely two-dimensional flow in the midspan region and the vortex-dominated flow near the hub.

The upper half of Fig. 8 is qualitatively a mirror image of the lower half because of the intersection of the stator and the outer casing. The passage vortex associated with the casing has a sense of rotation that is opposite to the sense of rotation of the hub passage-vortex. Hence, it induces a downward flow on the stator suction surface. This downward motion extends almost all the way to midspan. The casing passage-vortex, just like the hub passage-vortex, is pulled toward the hub because it contains low total pressure fluid. However, unlike the hub passage-vortex, which gets confined to the hub region because of its downward motion, the casing passage-vortex gets elongated and thus affects a greater portion of the stator surface. The midspan flow on the suction side is largely two-dimensional.

Figure 9 shows limiting streamlines on the stator pressure side. The flow on this side is seen to be almost two-dimensional everywhere except near the end-walls in the vicinity of the leading edge (where the incoming boundary layer separates

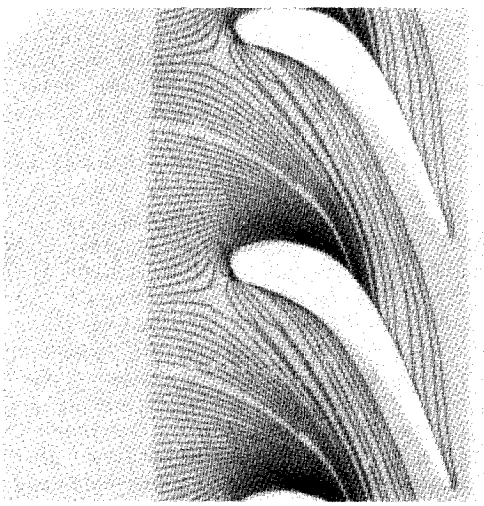

Fig. 7 Time-averaged limiting streamlines on the stator hub.

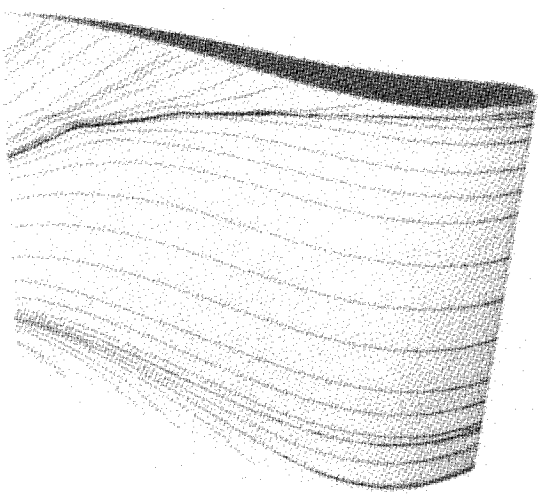

Fig. 8 Time-averaged limiting streamlines on the suction side of the stator.

and forms a horseshoe vortex). These observations are once again in close agreement with those reported in Ref. 7.

Figure 10 depicts limiting streamlines on the rotor-hub surface. The streamlines in this figure and in the following figures pertaining to the rotor were generated using rotor-relative velocities. As in the case of the stator, there is evidence of leading-edge separation and the formation of a horseshoe vortex. The secondary flow in the rotor passage is much stronger than the secondary flow in the stator passage. The rotor-passage flow is not aligned with the passage, but has a large tangential component. Hence it can be expected that the passage vortex impinges on the rotor suction side at a large angle and thus creates a local stagnation region. This would explain the higher pressures at midchord on the suction side of the rotor (Fig. 3a). The saddle point of separation, the attachment lines, and the detachment lines are all clearly discerned in Fig. 10. Another feature that can be seen in this figure is a line of separation on the suction side that extends from about 30% chord all the way to the trailing edge of the rotor.

The rotor suction-side limiting streamlines are shown in Fig. 11a. As in the case of the stator, the end-wall passage vortices induce strong radial components in the surface velocity field. The figure clearly shows the two lines of separation caused by the endwall passage vortices. Unlike the case of the stator, these two separation lines tend to move toward each other and the midspan region. The surface features mentioned above are in agreement with the experimental results of Ref. 8, which are shown in Fig. 11b. One difference between the experimental results shown in Fig. 11b and the numerical results of Fig. 11a is that the spanwise location along which the radial component of velocity is zero occurs at about 50% span in Fig. 11b and at about 65% span in Fig. 11a, probably a result of the aspect ratio of the rotor used in this study being smaller than that of the experimental rotor.

Figure 12a shows limiting streamlines on the rotor pressure side. In the first 30% of the chord from the leading edge there is a strong radial outflow. This has been demonstrated in Ref. 8 to be a result of the "relative-eddy" effect. This eddy is the axial component of the relative vorticity in the flow when viewed from the rotating frame of reference. Additional details regarding the relative-eddy effect can be found in Ref. 8. The flow in the latter 50% chord of the airfoil is almost two-dimensional. Figure 12b shows experimentally obtained surface-flow visualization for the same rotor.[8] There is good agreement between the numerical results of Fig. 12a and the experimental data of Fig. 12b.

Figure 13 shows the velocity vectors just above the rotor tip in the clearance region. In the first half of the rotor (toward the leading edge) the clearance flow is almost perpendicular to the pressure-side edge, whereas in the second half of the airfoil

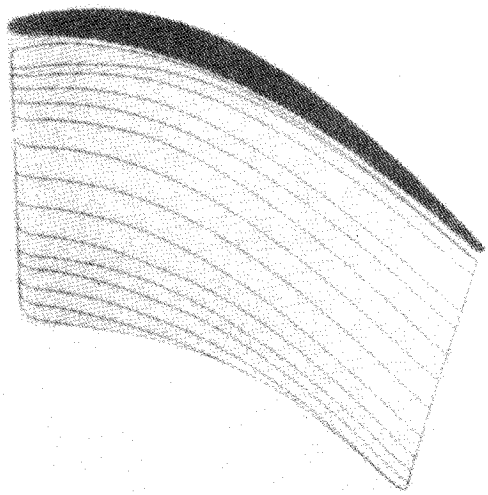

Fig. 9 Time-averaged limiting streamlines on the pressure side of the stator.

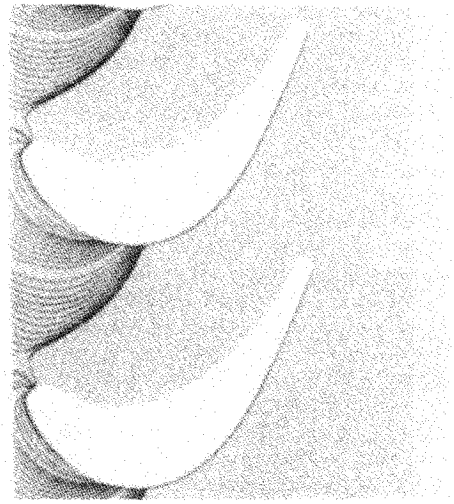

Fig. 10 Time-averaged limiting streamlines on the rotor hub.

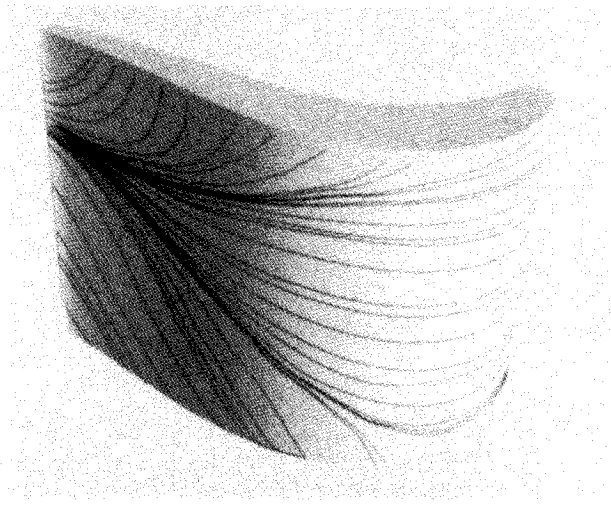

Fig. 11a Time-averaged limiting streamlines on the suction side of the rotor.

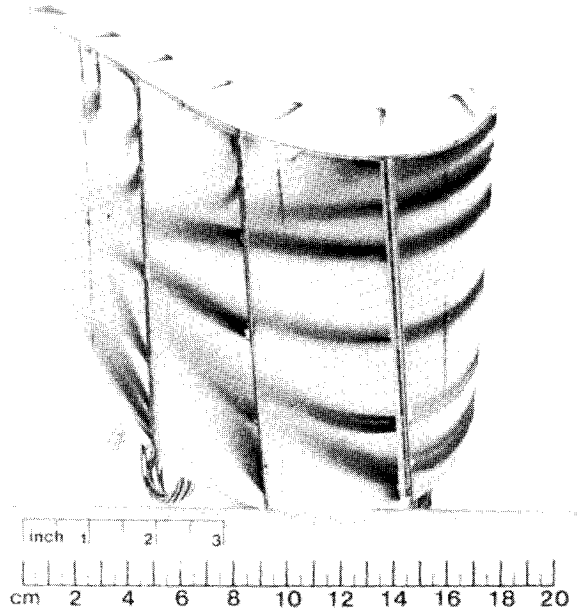

Fig. 11b Experimental visualization of rotor suction side flow.

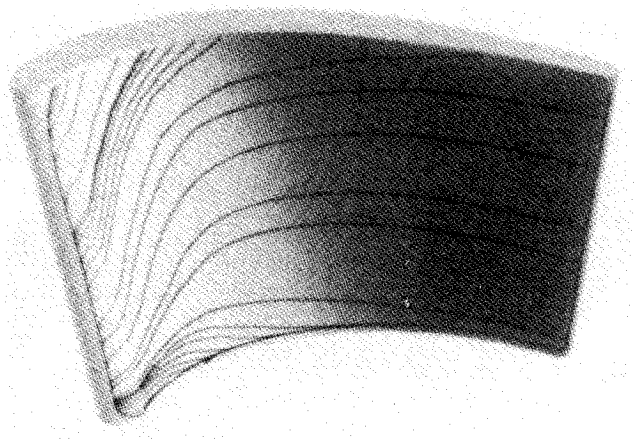

Fig. 12a Time-averaged limiting streamlines on the pressure side of the rotor.

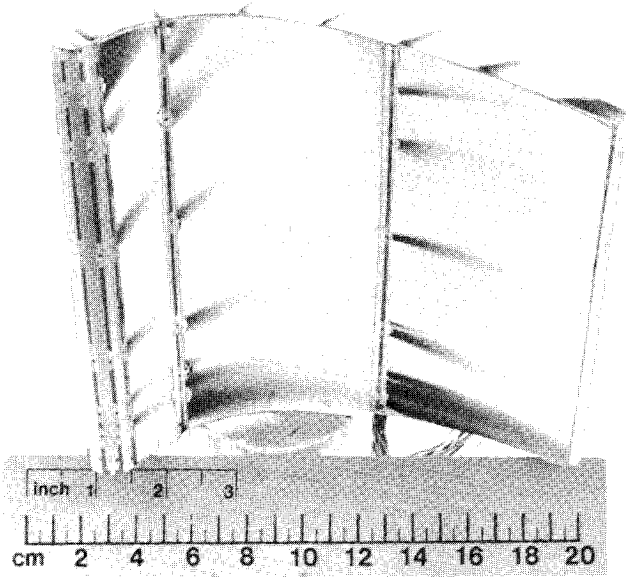

Fig. 12b Experimental visualization of rotor pressure side flow.

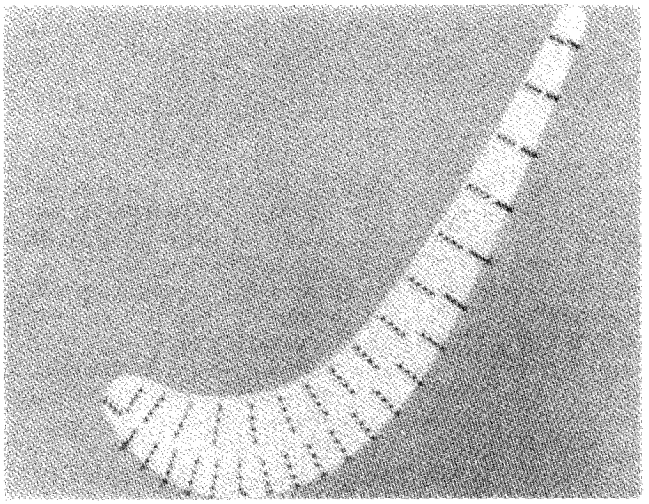

Fig. 13 Time-averaged flow directions in the rotor-tip clearance region.

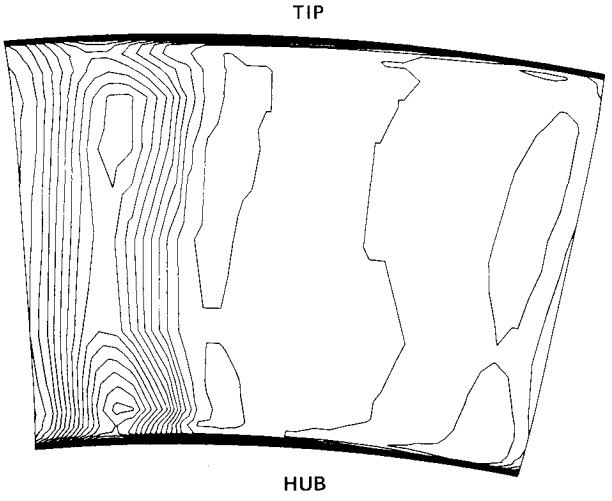

Fig. 14 Total-pressure contours at the exit to the stator airfoil (in a plane perpendicular to the hub axis).

the clearance flow is seen to be more inclined toward the positive axial direction. These features are in agreement with the experimental results shown in Fig. 12b.

Total-Pressure Contours at the Exit to the Stator and Rotor

The limiting streamlines and near-surface velocity vectors presented above demonstrate the effect of the stator- and rotor-generated passage vortices on the flow. A better understanding of the vortex structure can be obtained by looking at contours of total pressure at the exit to the stator and the exit to the rotor. The passage vortices contain fluid from the end-wall boundary layers and the airfoil surface boundary layers and, therefore, represent low total-pressure regions (compared with freestream total-pressure values). The difference in vortex total pressures and freestream total pressure enables one to clearly observe the passage-vortex structure by studying total-pressure contours at appropriate locations.

Figure 14 shows time-averaged, total-pressure contours, in the absolute frame of reference, at the exit to the stator (8.8% of the stator chord behind the stator trailing edge). This figure clearly shows three distinct entities: the hub passage-vortex, the casing passage-vortex, and the wake of the stator. The hub passage-vortex is seen to be confined to a region close to the hub, whereas the casing passage-vortex is elongated and occupies a relatively larger portion of the span. The reason for this difference in structure between the two vortices has already been discussed. Figure 14 also shows the end-wall boundary layers in the form of highly clustered total-pressure contours at the lower and upper boundaries, respectively.

Time-averaged, total-pressure contours (in the rotating frame of reference) just behind the rotor are depicted in Fig. 15. The contours are displayed on a plane perpendicular to the axis of the hub and at a distance of 7.4% of the rotor chord behind the trailing edge of the rotor. The end-wall passage vortices seem to have merged into a single low total-pressure region with its center at about 60% span. The experimental results of Ref. 9 do not indicate such a merger. This apparent merger of the low total-pressure regions in the numerical simulation is most probably because of the sparsity of grid points in the spanwise direction (in the midspan region). A total of 25 grid points were used in the spanwise direction to resolve the two endwall boundary layers and the region in between them. At least twice as many grid points are required for an adequate resolution in the spanwise direction. A calculation with a higher spanwise grid density is currently being planned. Figure 15 also shows the tip-leakage vortex just above the passage vortices. As in the case of the stator exit plane, the end-wall boundary layers are clearly seen at the upper and lower boundaries, respectively.

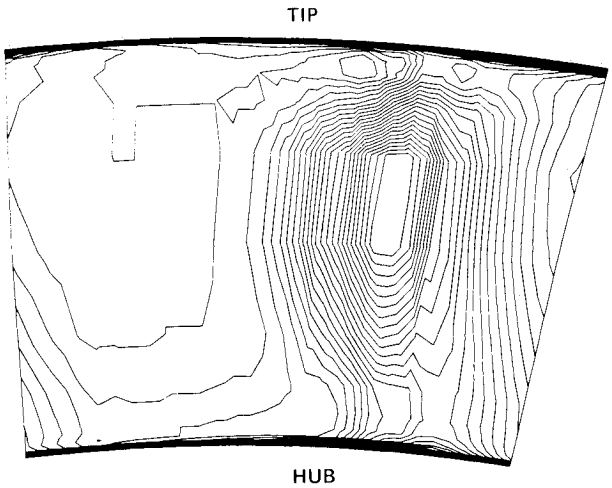

Fig. 15 Total-pressure contours at the exit to the rotor airfoil (in a plane perpendicular to the hub axis).

Areas for Future Research

One of the main differences between the experiment of Ref. 1 and the current numerical calculation is the use of an enlarged rotor airfoil in the present study so as to permit a one-stator/one-rotor simulation. This modification to the rotor changed the aspect ratio and, in the process, the blade-twist angles and other parameters that were discussed earlier. The use of an equal number of rotor and stator airfoils (instead of the actual airfoil count) results in unsteady pressure waves that are different from the actual ones, thus distorting the transient pressures and loads on the airfoil surfaces. The computer code used to simulate the results presented in this study is currently being modified to simulate an arbitrary number of rotor and stator airfoils. Such an extension has already been made to the two-dimensional single-stator/single-rotor code of Ref. 2, and the results obtained from the modified code are presented in Ref. 6.

The second problem that needs to be addressed is the turbulence model. Experience indicates that an algebraic turbulence model does not accurately predict eddy viscosities in regions of separation and in wakes without requiring extensive fine-tuning of the model. Hence, it is important to use a more generally applicable turbulence model, such as the two-equation models. Preliminary investigations with the two-dimensional code of Ref. 2 show that the $K-\epsilon$ turbulence model yields more accurate estimates of the eddy viscosity in the separation regions near the trailing edges of the blades and, hence, results in smaller pressure fluctuations. Another problem area with regard to turbulence modeling is the tip clearance region. Currently, the values of eddy viscosity in the tip-clearance region are set to zero. More generally applicable turbulence models, such as the one of Ref. 10, may yield realistic eddy-viscosity values for the clearance region.

One of the main problems in simulating unsteady three-dimensional flow in complex geometries such as turbomachinery is the large amount of computer time required to obtain accurate solutions. Until these computing times are reduced by an order of magnitude or more, three-dimensional, multirotor/multistator codes will only serve as research tools used to understand the basic flow mechanisms; they will not be used in the design process. Various improvements in linearization techniques that will permit larger time-steps are currently being investigated to minimize computing times.

Inlet and exit boundary conditions affect the transient solution in the interior of the domain. Although nonreflective boundary conditions can be developed, it is not clear whether these boundary conditions will result in more accurate simulations in all cases. This is because in real situations the first stage may be followed by another stage, or the flow may exit through a nozzle to the ambient, or it may encounter bends in the piping, to mention just a few of the possibilities. Simulating entire systems such as multistage turbomachinery with the appropriate upstream and downstream conditions will require far more computing power than is currently available. Hence, the area of inlet and exit boundary conditions still requires development.

Summary

An unsteady, thin-layer, Navier-Stokes code to study three-dimensional rotor-stator interaction problems has been developed. The hub, outer casing, and rotor-tip clearance are all an integral part of the code. The code was used to simulate subsonic flow past a turbine stage for which considerable data exist.

Results in the form of time-averaged surface pressures, surface-pressure amplitudes (corresponding to the pressure fluctuation in time), limiting streamlines for various surfaces, near-surface velocity vectors, pressure contours in the stator and rotor rows, and total-pressure contours at the exit to the stator and rotor have been presented. Time-averaged pressures from hub to tip are compared with experimental data. Comparisons with experimental data are also made for midspan pressure amplitudes and rotor-surface velocities. In all cases the numerical data compared well with the experimental data.

The problem areas to be addressed in the future are 1) the use of multiple airfoils in the calculation, 2) the use of better and more generally applicable turbulence models, and 3) the development of improved inlet and exit boundary procedures that can simulate a variety of inlet and exit conditions.

Acknowledgments

I would like to thank Dr. R. P. Dring of United Technologies Research Center for providing the airfoil geometries and the experimental data. I am especially grateful to him for the encouragement and many helpful suggestions he has provided during this study and for help in interpreting the numerical data. I would also like to thank Mr. P. Kelaita of Sterling Software for providing the graphical support for the project. Thanks are also due to The Air Force Office of Scientific Research for permitting me to use some of the experimental data presented in this study, and to NASA Lewis Research Center for partially supporting the project.

References

[1]Dring, R. P., Joslyn, H. D., Hardin, L. W., and Wagner, J. H., "Turbine Rotor-Stator Interaction," *Journal of Engineering for Power,* Vol. 104, Oct. 1982, pp. 729–742.

[2]Rai, M. M., "Navier-Stokes Simulations of Rotor-Stator Interaction Using Patched and Overlaid Grids," *Journal of Propulsion and Power,* Vol. 3, Sept.-Oct. 1987, pp. 387–396.

[3]Baldwin, B. S. and Lomax, H., "Thin Layer Approximation and Algebraic Model for Separated Turbulent Flow," AIAA Paper 78-257, January 1978.

[4]Hung, C. M. and Buning, P. G., "Simulation of Blunt-Fin-Induced Shock-Wave and Turbulent-Layer Interaction," *Journal of Fluid Mechanics,* Vol. 154, 1985, pp. 163–185.

[5]Joslyn, H. D. and Dring, R. P., "Experimental and Analytical Study of Turbine Temperature Profifle Attenuation," Air Force Office of Scientific Research, Contract F49620-86-C-0020, Aug. 1988.

[6]Rai, M. M. and Madavan, N. K., "Multi-Airfoil Navier-Stokes Simulation of Turbine Rotor-Stator Interaction," AIAA Paper 88-0361, Jan. 1988.

[7]Langston, L. S., Nice, M. L., and Hooper, R. M., "Three-Dimensional Flow Within a Turbine Cascade Passage," *Journal of Engineering for Power, Transactions of the ASME,* Vol. 99, Jan. 1977, pp. 21–28.

[8]Dring, R. P. and Joslyn, H. D., "The Relative Eddy in Axial Turbine Rotor Passages," American Society of Mechanical Engineers, Paper 83-GT-22, 1983.

[9]Dring, R. P. and Joslyn, H. D., "Measurements of Turbine Rotor Blade Flows," *Journal of Engineering for Power, Transactions of the ASME,* Vol. 103, April 1981, pp. 400–405.

[10]Chien, Kuei-Yuan, "Predictions of Channel and Boundary-Layer Flows with a Low-Reynolds-Number Turbulence Model," *AIAA Journal,* Vol. 20, Jan. 1982, pp. 33–38.